Generating high-temporal and spatial resolution TIR image data

Herrero-Huerta, M.; Lagüela, S.; Alfieri, S. M.; Menenti, M.

DOI
10.1016/j.jag.2019.01.016

Publication date
2019

Document Version
Final published version

Published in
International Journal of Applied Earth Observation and Geoinformation

Int J Appl Earth Obs Geoinformation 78 (2019) 149–162

Contents lists available at ScienceDirect

Int J Appl Earth Obs Geoinformation

journal homepage: www.elsevier.com/locate/jag

Generating high-temporal and spatial resolution TIR image data

M. Herrero-Huerta[a,b,c,*], S. Lagüela[b,e], S.M. Alfieri[a], M. Menenti[a,d]

[a] Department of Geoscience and Remote Sensing, Delft University of Technology, 2628 CN Delft, the Netherlands
[b] Department of Cartographic and Land Engineering, University of Salamanca, Higher Polytechnic School of Avila, Hornos Caleros 50, 05003 Avila, Spain
[c] Department of Agronomy, Purdue University, IN 47906, USA
[d] Remote Sensing and Digital Earth Institute, Chinese Academy of Sciences, Beijing 100101, China
[e] Applied Geotechnologies Research Group, University of Vigo, Mining and Energy School, Campus Universitario Lagoas-Marcosende, 36310, Vigo, Spain

ARTICLE INFO

Keywords:
Data fusion
Image processing
Thermal infrared data
Multi-sensor system
Spectral unmixing

ABSTRACT

Thermal InfraRed (TIR) image data at high temporal and spatial resolution are required to monitor the rapid development of crops during the growing season, taking into account the fragmentation of most agricultural landscapes. Moreover, integrating high-resolution satellite TIR data to calibrate hydrological models is a powerful information to efficiently monitor crop water use. Conversely, no single sensor meets these combined requirements in the TIR spectral region. Data fusion approaches offer an alternative to exploit observations from multiple sensors, providing image data to meet the combined requirements on spatial and temporal resolution.

A novel spatio-temporal data fusion workflow based on a multi-sensor multi-resolution algorithm was developed and applied to generate TIR synthetic image data at high temporal and spatial resolution. The workflow includes two steps: in the first step, synthetic daily radiance images at Top of Atmosphere (TOA) and 30-m spatial resolution (at the ground) are generated using TIR radiometric data at TOA collected by the Moderate Resolution Imaging Spectroradiometer (MODIS) daily 1-km and Landsat 8/TIRS 16-day 30-m. This procedure is applied to two image pairs on different dates. The workflow yields an estimator to generate TIR TOA radiance data on any given date, provided a MODIS radiance image is available. The next step applies constrained unmixing of the 30 m (now considered as low-resolution) TIR images using the information about sub-pixel land-cover obtained from co-registered images at higher spatial resolution in the VNIR (Visible Near InfraRed) spectrum. In our case study, the L8/TIRS synthetic image data were unmixed to the Sentinel 2/MSI with 10 m × 10 m spatial resolution. Two geographically diverse experiments were carried out using the same procedure: one in The Netherlands to evaluate the procedure and other in Puglia (Italy) to generate a time series of the 10-m × 10-m TIR image data product. The validation experiment, where an actual TIRS image was applied as a reference, gave a RMSE value of 35.3 W/(m^2 μm sr), which corresponds to a relative value of 8.5% against the TIRS reference values. The results confirm the feasibility of the proposed methodology, which yields a synthetic thermal band to integrate with the multi-spectral data provided by the S2/MSI at 10 m resolution.

1. Introduction

Thermal InfraRed (TIR) data is critical to model surface energy balance (Alfieri et al., 2013), evapotranspiration and surface moisture (Carlson, 2007) and climate change (Weng, 2009). Biophysical variables, such as water stress, grain yield (Smigaj et al., 2017; Elsayed et al., 2017; Guo et al., 2016) and land-cover changes (Ning et al., 2017) can be retrieved from TIR radiometric data alone or in combination with other spectral bands such as visible (Zhong et al., 2017). A recent effort has been focused on using remotely sensed Land Surface Temperature (LST) to calibrate hydrological models by modifying soil parameters, such as hydraulic conductivity and improving the understanding of the model internal variables (Corbari and Mancini, 2014). LST image data can be used for the calibration of distributed hydrological models (Corbari and Mancini, 2014). A combined calibration based on satellite LST and in-situ measurements of flow-rate (Fig. 1) is potentially an effective way to estimate flow-rates over time and spatially distributed maps of representative equilibrium temperature and evapotranspiration. Retrieval of LST from TIR radiometric data is well established and alternate algorithms are well documented (Sobrino and Jiménez-Muñoz, 2005). Moreover, the relationship between LST and diverse spectral indexes suggests an opportunity to improve spatial and

* Corresponding author at: Department of Geoscience and Remote Sensing, Delft University of Technology, 2628 CN Delft, the Netherlands.
E-mail addresses: mherrero@purdue.edu, monicaherrero@usal.es (M. Herrero-Huerta), susiminas@uvigo.es, sulaguela@usal.es (S. Lagüela), s.m.alfieri-1@tudelft.nl (S.M. Alfieri), m.menenti@radi.ac.cn, m.menenti@tudelft.nl (M. Menenti).

https://doi.org/10.1016/j.jag.2019.01.016
Received 8 June 2018; Received in revised form 23 January 2019; Accepted 28 January 2019
Available online 13 February 2019
0303-2434/

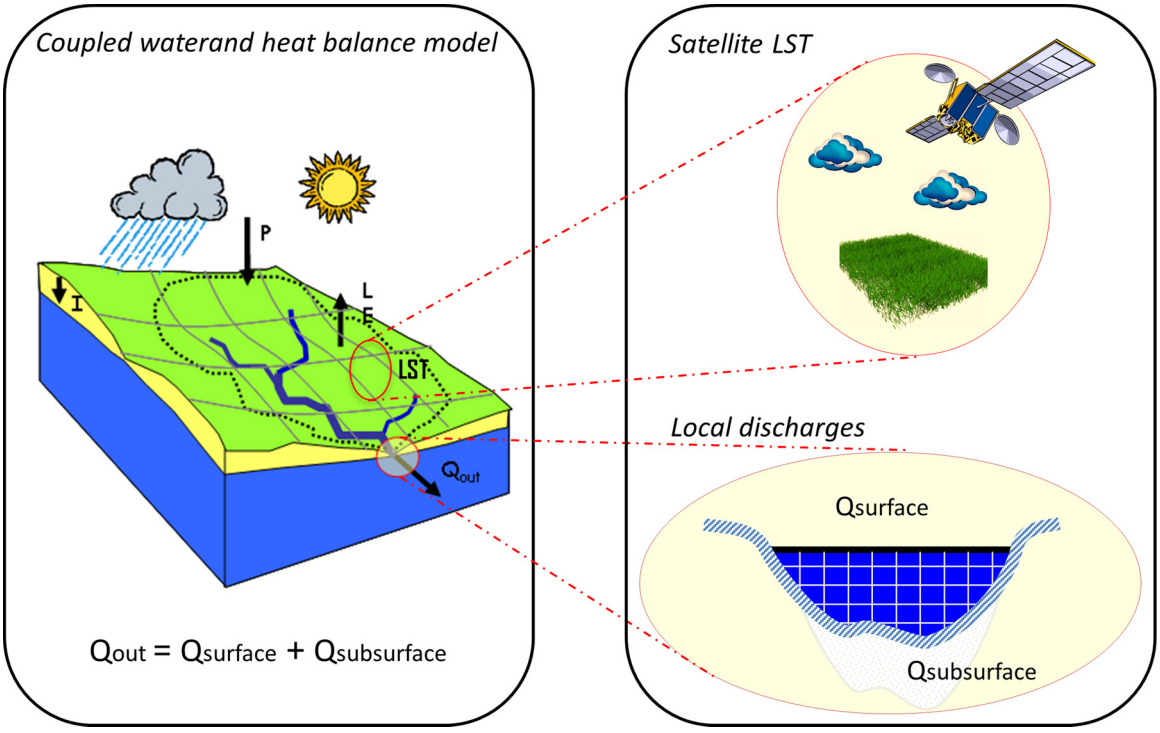

Fig. 1. Conceptual approach to the calibration of a coupled water and heat balance model using observations of LST.

temporal resolution of current TIR image data (Yue et al., 2007; Julien et al., 2011).

Due to technical and financial constraints, no single sensor provides TIR data with both high spatial and temporal resolution (Price, 1994). Frequent temporal sampling is essential to detect rapid surface changes, very relevant in crop-growth monitoring and intra-seasonal ecosystem disturbance (Shabanov et al., 2003). High spatial resolution is compulsory in land-oriented applications to minimize the impact of mixed pixels in mapping land cover and interpret its spatial variations. For example, a minimum sample size of three pixels was deemed necessary to obtain reliable TIR measurements of river temperatures (Handcock et al., 2006), which implies that the water temperature in rivers narrower than 180 m cannot be measured with Landsat ETM + (given that the original product has a 60-m spatial resolution).

Data-fusion models can be applied to generate synthetic data by integrating high spatial and temporal resolution data acquired by diverse sources and sensors (Herrero-Huerta et al., 2016). Data fusion must preserve the radiometry of the data being combined to meet the requirements of applications. This applies to e.g. quantitatively derive radiometry changes caused by phenology (Stathopoulou and Cartalis, 2009), determine soil freeze-thaw status in critical ecological areas (Kou et al., 2017) and determine the presence and severity of urban heat islands (Mukherjee et al., 2017).

The remote-sensing community has developed two well-documented approaches to do spatial and temporal data fusion from two sensors, respectively. The Spatial and Temporal Adaptive Reflectance Fusion Model (STARFM) proposed by Gao et al. (2006) is widely applied to generate synthetic daily Landsat image data by combining several pairs of concurrent Landsat and MODIS images and one MODIS image on the day of each synthetic image, towards temporal data fusion. This approach was originally designed for reflectance images in the visible and near infrared (NIR) bands, which are highly correlated with the surface type (Richter et al., 2006). To apply the same approach to thermal infrared data, the Annual Temperature Cycle (ATC) and even the daily temperature cycle (Weng et al., 2014), need to be determined when correlating data acquired at different times. Regarding spatial data fusion from satellite images from the same date, existing thermal sharpening techniques disaggregate at-sensor radiance by capturing spatial patterns with image data at shorter wavelengths and higher spatial resolution (Dominguez et al., 2011). These multi-resolution image fusion techniques use various deterministic or statistical predictors (Zhukov and Oertel, 1996) and use VNIR (Visible Near InfraRed) bands as a reference Bangira et al. (2017a), e.g. L8/OLI at 30 m and for S2/MSI at 10–20 m (Kim et al., 2013). When the focus is set on the TIR band and the incorporation of LST from one sensor to the VNIR bands of a different sensors, fewer works can be found. (Wu et al., 2015) proposed a method able to fuse the LST from arbitrary sensors in an unified framework. Specifically, a spatio-temporal integrated temperature fusion model for the retrieval of high temporal and spatial resolution LST from multi-scale polar-orbiting and geostationary satellite observations was developed. Mukherjee et al. (2014) analyzed different downscaling methodologies, based on regression models between LST and NDVI (Normalized Different Vegetation Index) as auxiliary data. The difference between methodologies stays in the regression models used, from 2nd order polynomial (DisTrad (Kustas et al., 2003)) to least mean square regression (LMSDS). For each thermal image from a satellite sensor, images in different spectral bands from the same sensor are used to calculate NDVI and applied to downscale. In addition to NDVI, other parameters can be used for downscaling, provided they present a linear relation with LST; their selection depends on the application. This way, (Bechtel et al., 2012) applied 29 parameters, including topography from SAR measurements (Synthetic Aperture Data), Mean Annual Surface Temperature and land cover data, to downscale LST for urban monitoring applications. In contrast, (Pan et al., 2018) developed a new parameter, Normalized Sand Difference Index, to downscale LST data in desert areas. Thus, the regression methodologies work based on the assumption that RGB and NIR channels present finer spatial resolution than TIR channel, for every satellite sensor. Thus, the regression with LST is calculated at coarse resolution and then applied to the computation of the new fine-resolution pixels. A review of existing methods to downscale LST to subpixel level and allow its use in applications requiring high both spatial and temporal resolutions can be found in (Zaksek and Ostir, 2012).

In this study a new data fusion algorithm was developed to generate

synthetic TIR data at TOA at 10-m and high temporal resolution. In the first step, L8/TIRS (Thermal Infrared Sensor) and MODIS/TIR data, both at TOA, are blended to obtain TIR data at 30-m and high temporal resolution. The method applies an adaptive radiative model based on spectral similarity, i.e. the Linear Spectral Mixture Analysis (LSMA). After that, the spatial resolution is improved to 10-m, using the visible bands of S2/MSI as reference to apply spatial unmixing: their use is direct, with no intermediate computation of parameters. We designed our methodology to be applicable to TOA radiometric data acquired by different sensors and satellites to avoid the impacts of variable atmospheric conditions in the data fusion. Retrieval of LST is carried out once the synthetic TIR images at high spatial and temporal resolution are generated. This last step is not addressed in this paper.

The paper is organized as follows: after this brief introduction, the proposed methodology is described in Section 2. Next, the results and their evaluation are presented in Sections 3 and 4, respectively. Section 5 includes a discussion of the results. Finally, the conclusions are highlighted.

2. Methods and materials

2.1. Methods

The proposed approach was designed to generate high temporal and spatial resolution synthetic TIR data based on a multi-sensor multi-resolution technique (MMT). Fig. 2 summarizes the workflow and the data products generated by the method proposed, explained in detail below. At the top of Fig. 2, step 1 shows the construction of the blender algorithm using two pairs of MODIS and L8 / TIRS images at t_1 and t_2 to generate a synthetic L8 / TIRS image at t_3; at the bottom, step 2 illustrates the unmixing of the synthetic L8 / TIRS image at t_3 using a S2 / MSI; the bottom panels shows on the left a color composite of MSI Bands 842 nm, 560 nm and 490 nm and on the right the synthetic 10 m TIR image.

Our methodology includes two different steps: the first one deals with the temporal resolution, while the second one with the spatial resolution. In the first step, MODIS and Landsat radiometric data have been used in this study, but any other image data could be used. TIR radiometric data at TOA on two different dates (t_1 and t_3 in Fig. 2) are used, i.e. MODIS/TIR daily 1-km and L8/TIRS 16-day sampled at 30-m resolution. Specifically, the L8/TIRS data are acquired with an IFOV of 142 μrad, which gives a footprint of approximately 100*100 m, as L0R/L1R data with irregularly shaped and spaced pixels and resampled by cubic convolution to L1G, L1GT and L1 T data products with 30*30 m pixels. Thus, individual measurements are done with a footprint 100*100 m but the L1G, L1GT and L1 T data products are generated by interpolating (cubic convolution) the L1R data and terrain corrected using 30*30 m DEM. L1 T data product we used has a spatial resolution of 30*30 m. In consequence, synthetic thermal radiance images at TOA at 30-m spatial resolution on any required date (t_2 in Fig. 2) between t_1 and t_3 are generated. The evolution of thermal conditions between t_1 and t_3 must be parameterized. The maximum time interval tested with accurate results between t_1 and t_3 is 4 months. In this step, an estimator (Eq. 2) of L8/TIRS radiance is constructed by using two pairs of MODIS and TIRS image data on two different dates, which can be rather far apart. In other words, the estimator is assumed invariant in between these two dates. To correct for the annual evolution of TOA radiance, we have applied first the algorithm HANTS to model the yearly time series. These values are then subtracted from the MODIS TOA observations to give a time series where temporal signals are due to short term variations in atmospheric forcing and surface conditions. The estimator reconstructs the spatial pattern in the TIRS data using the MODIS/TIR data as a predictor. If applied to BOA radiance or LST image data, both the model of the yearly time series obtained with HANTS and the estimator constructed with STARFM depend on the evolution of atmospheric conditions. This problem is mitigated if our method is applied to TOA radiance data limiting the challenge of atmospheric correction to the retrieval of LST for the final very high spatial resolution thermal infrared image.

Concretely, step 1 (see Fig. 2) can be described as follows:

- TIR data acquired by different sensors at different times, are radiometrically calibrated and geometrically rectified so that all TOA radiometric data are consistent spatially and temporally (Masek et al., 2006). Nevertheless, factors as acquisition time, bandwidth, orbit parameters, geolocation errors, effective pixel coverage and spectral response function, generate random and systematic differences in data acquired by different sensors. An extra-filter is applied to remove poor quality observations and to retain cloud-free pixels.
- TIR data at lower and higher spatial resolution are acquired at different times and need to be corrected for intra-annual variability to make the radiometric measurements comparable. To do that, the yearly cycle in TOA radiance is modelled by reconstructing a full yearly MODIS/TIR time series of daily observations. This is done by applying the HANTS algorithm (Menenti et al., 1993; Zhou et al.,

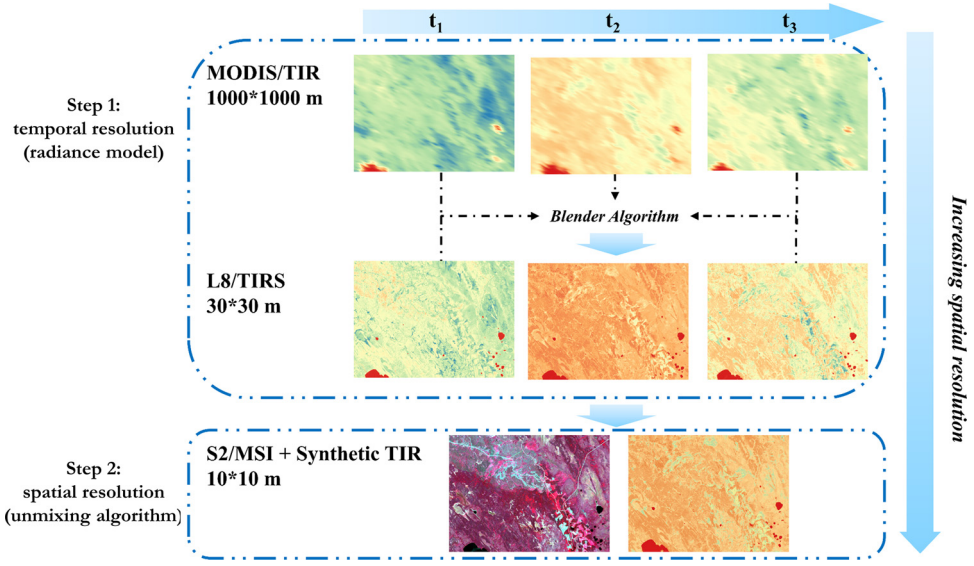

Fig. 2. Conceptual workflow of the proposed temporal and spatial data fusion algorithm.

2016) to daily MODIS/TIR data from 2016. The TOA cycle gives the yearly evolution of TIR radiance for each pixel. Because of the image size, the reconstruction is done for all pixels within a moving window at the same time. The algorithm combines harmonic analysis with curve fitting in iterative steps. For each pixel, the signal is modelled using a Fourier series:

$$y(t) = a_0 + \sum_1^{n_f} (a_i \cos(2\pi f_i t) + b_i \sin(2\pi f_i t)) \quad (1)$$

where n_f is the number of frequencies, a_0 is the average of the series and t the time of observation. The coefficients a and b are the coefficients of trigonometric components functions at the frequency i, calculated for each pixel.

- Linear Spectral Mixture Analysis (LSMA) is applied to the TOA radiometric data to represent MODIS radiometric data as a linear combination of L8/TIRS radiometric data (within each MODIS pixel), weighted by the fractional abundance, based on land cover, of each pixel component (Zurita-Milla et al., 2008). We estimate the temporal variation in radiance within the MODIS data as the weighted sum of L8/TIRS radiance changes for each land cover type within each MODIS pixel. The procedure to blend the MODIS and L8/TIRS radiometric data is detailed below, following the STARFM approach (Gao et al., 2006):

a) L8/TIRS images at t_1 and t_3 are used to search for pixels with radiance value similar to the value of a central pixel in a local window. The size of the moving window size is defined by the radiance homogeneity in the L8/TIRS data, i.e. a smaller window may be applied in a relatively homogenous scene. A window size of 15*15 pixels in L8/TIRS data was found as an accurate compromise between the processing time and the homogeneity in radiance for this sensor in the tested areas. A threshold is estimated on the basis of the standard deviation in the L8/TIRS scene and the number of land cover classes within the search window applied to the L8/TIRS mages. In this way, only values from similar pixels within the L8/TIRS local window are used to build the estimator.
b) Next, a normalized weight function that expresses the contribution of the similar pixels to the central pixel within the local window is calculated. It is determined by the relative location of similar pixels and radiance value between L8/TIRS and MODIS data and by the temporal variation of MODIS radiance. This function is determined under the assumption that the fractional abundance of each land cover component within a MODIS pixel does not vary between t_1 and t_3.
c) Lastly, the synthetic L8/TIRS image at 30-m spatial resolution is obtained by constructing the estimator defined by Eq. 2 to each central pixel of the moving window to the MODIS data at the required date:

$$L(x_{s/2}, y_{s/2}, t_2) = \sum_{k=i}^{P=2} \sum_{i=1}^{N} W_{ik} * (L(x_i, y_i, t_k) + (M(x_i, y_i, t_2) - (M(x_i, y_i, t_k)) \quad (2)$$

where L denotes TIRS radiometric data, M by MODIS, W_{ik} is the normalized weight function, s represents the size of the moving search window, being $(x_{s/2}, y_{s/2}, t_2)$ the coordinates of the central pixel at the prediction time, P defines the number of paired TIRS/MODIS images (2 in our case study), N is the total number of similar TIRS pixels within the moving window and i is the index.

Eq. 2 prescribes that at each pixel of the synthetic TIRS image, the estimated TOA radiance at t_2 equals the observed TIRS radiance interpolated between t_1 and t_3, plus the sum with sign of the differences between t_2 and t_1, and t_2 and t_3, respectively, observed by MODIS for all similar pixels within the window in the MODIS image.

Step 2 (see Fig. 2) is now performed once the synthetic TIRS image on the required date is obtained. It consists in generating a second synthetic image at higher spatial resolution by estimating sub-pixel values. A linear unmixing algorithm is applied to the 30-m synthetic TIRS radiometric data using the information about the sub-pixel land-cover determined from co-registered images at higher spatial resolution. In our case study, the synthetic TIRS data at 30-m spatial resolution were unmixed to S2/MSI 10 m resolution. Thereby, our MMT algorithm yields 10 m spatial resolution synthetic data on the required date.

We assume that thermal infrared existence correlates with land cover and spectral reflectance in the VNIR region. Accordingly, clusters of pixels with similar VNIR reflectance are obtained by applying an unsupervised classification of the bands 2, 3 and 4 of S2/MSI in the entire area of study (Zhukov et al., 1999). The ISODATA (Iterative Self-Organizing Data Analysis Technique) classification algorithm (Ball and Hall, 1965) is applied by specifying the maximum number of clusters only. In order to avoid the occurrence of unclassified pixels, an adaptive search was implemented, where the class of each unclassified pixel is assigned as the most abundant class in its 3*3 pixel-neighborhood.

The 10-m TIR radiances are estimated within each 30-m TIRS pixel using a moving window. The main limitation is that same class pixels within the moving window are given the same TIR radiance at TOA and consequently some spatial variability in TIR radiance is lost for pixels in the same cluster within the moving window. On the other hand, the size of the moving window determines the maximum number of clusters that can be identified and applied to estimate the high resolution TIR radiance. Consequently, the size of the moving window affects the characterization of thermal variability. A 5-pixel moving window was found to be a good compromise between acceptable spatial averaging of LST within each high-resolution class and a sufficient number of low resolution pixels for a stable inversion of the system of equations (Xu et al., 2015). It should be noted that the function of the moving windows in step 1 and step 2 is completely different, thus their size have to be set independently because in step 1 the window is applied to construct the estimator in Eq. 2, while in step 2 is applied to classification and linear unmixing. Our unmixing algorithm assumes linearity of thermal radiance to calculate the contribution of each class to the low-resolution pixels. That is, for every 30-m resolution pixel the radiance is a linear combination of the radiances of the classes of the high-resolution pixels within the moving 5-pixel window (Nash and Sutcliffe, 1970) (Fig. 3 and Eqs. 3 and 4). This is another advantage to use TOA

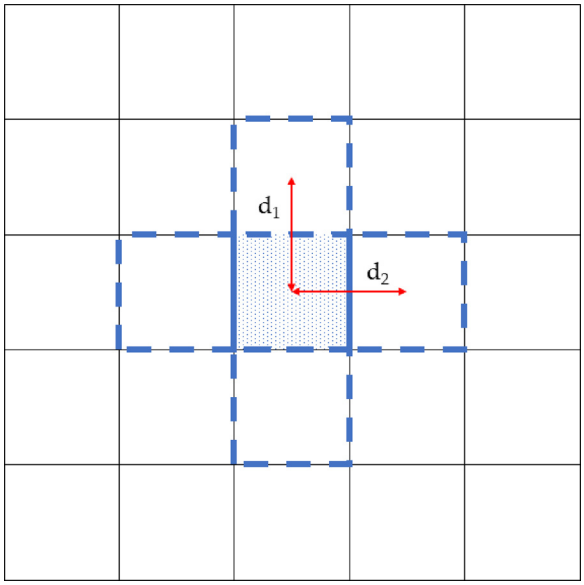

Fig. 3. Visualization of the 5-pixel moving window used for the unmixing step. As stated in the text, d_1 and d_2 are both equal to the pixel size, i.e. the 10-m of S2/MSI in our case study.

radiance in our approach, since linearity cannot be assumed for surface temperature values. Since all pixels in the 5-pixel moving window are at the same distance to the central pixel (except for the central pixel itself) due to their lateral adjacency to it (Fig. 3), the system is solved through unweighted least squares estimation.

Analytically, the 10-m resolution radiance values within each 30-m pixel are calculated by solving a linear system by least squares estimation (Eq. 3):

$$P_j(r, c) = \sum_{cl_i} f_i(r, c; cl_i) P_i^*(cl_i) \quad (3)$$

where $P_j(r, c)$ is the pixel radiance value (r, c) for the central pixel in the moving window (a 30-m TIRS pixel in our case study), $P_i^*(cl_i)$ is the radiance of class cl_i to be estimated and $f_i(r, c; cl_i)$ is the fractional abundance of class cl_i in the 10-m pixels within each 30-m resolution pixel, calculated as in Eq. 4.

$$f_i(r, c; cl_i) = \sum_{(f,g)\in(r,c)} n_{f,g;cl_i} / \sum_{(f,g)\in(r,c)} n_{f,g} \quad (4)$$

where $n_{f,g;cl_i}$ is the number of high resolution pixels of class cl_i within the moving window and $n_{f,g}$ is the total number of high resolution pixels within the moving window.

In Eq. 3, the resolution error of the linear combination is neglected. Thereby, the energy balance is maintained for the central pixel of the moving window, which is the one to be solved for each position of the window. For this reason, the unmixing algorithm used in among the "constrained" unmixing algorithm group.

2.2. Materials: case studies

Two geographically diverse case studies were carried out to test the proposed methodology, characterized by different climatic conditions, water availability, crop types, irrigation techniques and water distribution rules (Fig. 4). One case is an 11,500 km^2 area of The Netherlands where the approach was validated (Section 3.1). The other is a synthetic image time series during the irrigation season over a crop area in the north of Puglia (Italy) as a practical case to demonstrate the power of the methodology to calibrate hydrological models (Section 3.2).

In The Netherlands, the predominant wind direction is South-West, which causes a moderate climate with warm summers and cold winters and typically high humidity. The case study area is complex area with many different land cover types, including farmland, forest, bare soil, urban land, wetlands and water as identified by the Netherlands Environmental Assessment Agency (PBL). Dominant crops are grassland and maize and dominant arable crops are potatoes and sugar beet. Large parts are occasionally irrigated by sprinkling in response to drier spells, while subsurface drainage has been recently introduced with a rapid extension of its use. Water supply reaches the area via a system of channels with several inlets. Cropland patches are small and show distinct temporal patterns based on planting and harvest schedules and local environmental conditions such as soil water content, fertility and health. In this context, monitoring this crop growth requires high spatial resolution imagery to isolate particular fields and high temporal resolution imagery to track development.

In contrast, Puglia (Italy) has a typically Mediterranean climate with hot summers and warm winters and typically low humidity (water scarcity). The land cover is basically crops and urban lands, but bare soil, forest and water are as well included. The main crops are cereals and vegetables for fresh consumption. Asparagus, Swiss Chard, Leaf Beet, Savoy Cabbage, Fennel, Spinach among others are cultivated between September and April avoiding the hottest season. Vineyards and olive orchards are also present. Water is withdrawn from the deep aquifer with wells and stored in reservoirs. Irrigation is performed by drip or sprinkler methods. It is regulated by the Consortium for the Reclamation of the Capitanata which operates on 44,000 ha (from the

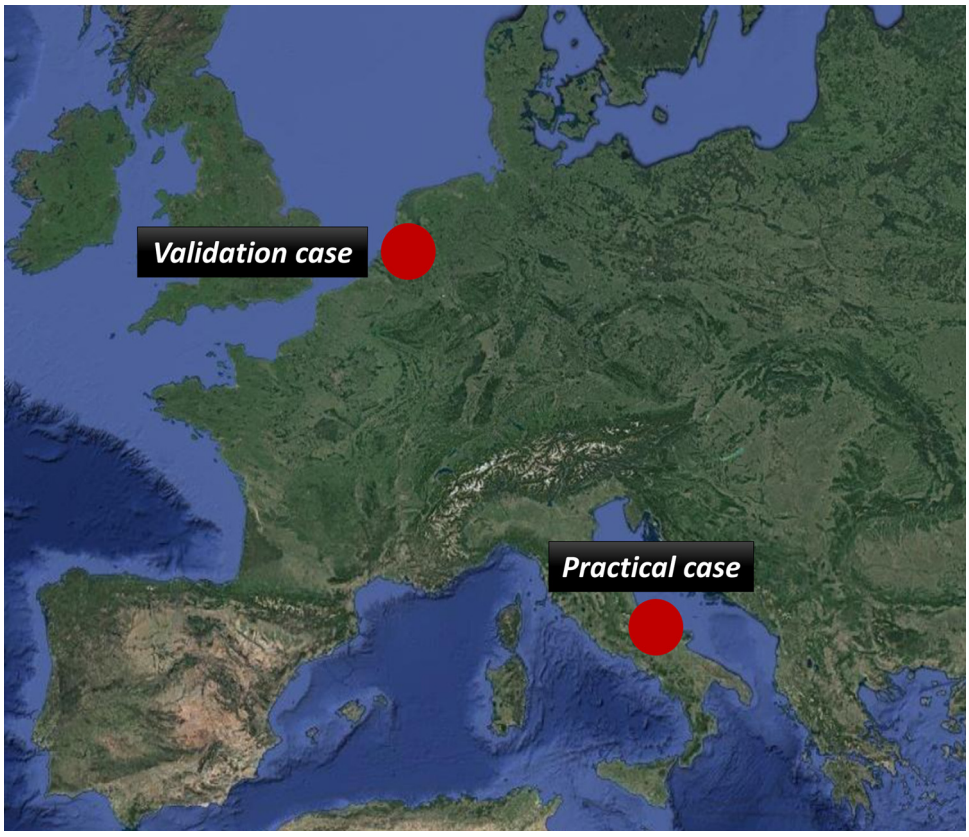

Fig. 4. Location of the two case studies carried out in Europe: validation in The Netherlands and demonstration in Italy *(based on FreeMapTools source)*.

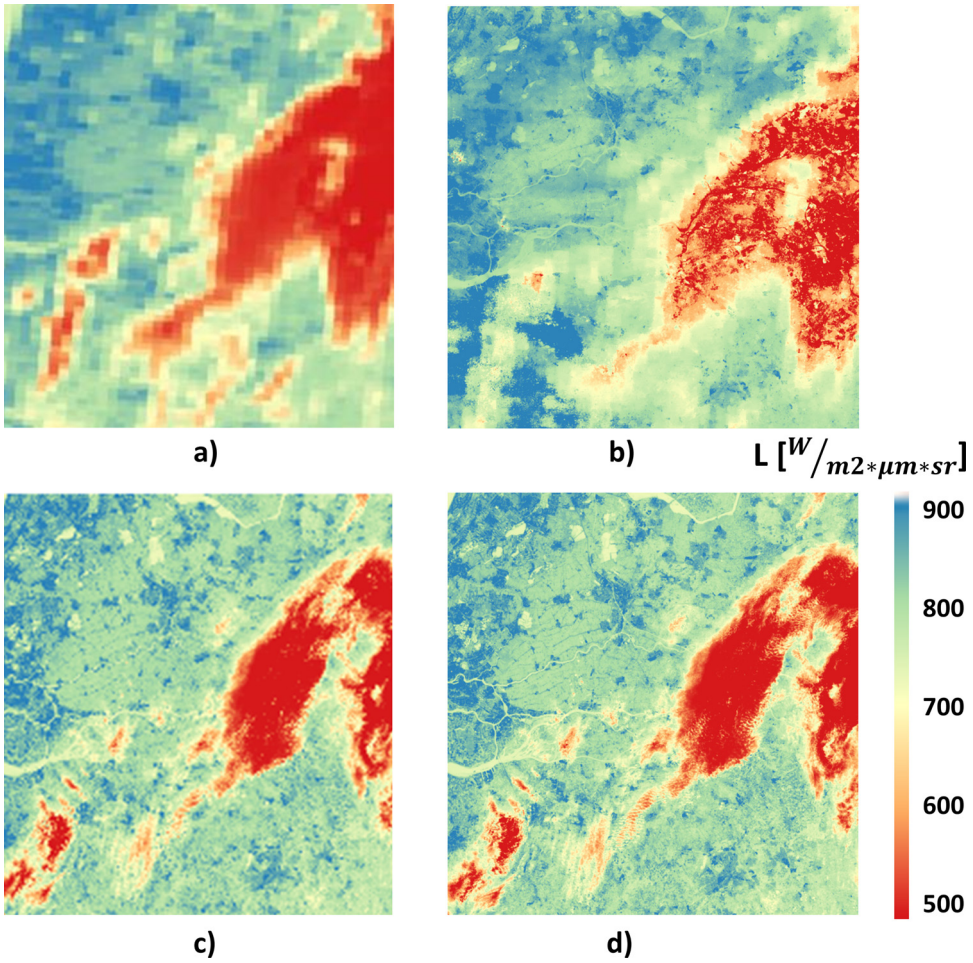

Fig. 5. TIR images of the test-site in The Netherlands on May 1 st 2016: a) MODIS/TIR at 1000-m resolution; b) synthetic L8/TIRS at 30-m resolution; c) actual L8/TIRS at 30-m resolution and d) synthetic TIR image data at 10-m resolution; (DL coordinates: 599960, 5,690,007; UR coordinates: 708046, 5,799,876; EPSG 32,631).

Saccione stream, which marks the border with Molise to the River Ofanto that delimits the province of Foggia from that of Bari).

3. Results

3.1. Validation case: The Netherlands

The proposed approach was tested over an area of 115*100 km^2 in the South-East of The Netherlands. It is mainly flat, with gentle slopes from the south to the north.

L8/TIRS level 1 T geotiff product, band 10, at 30 m resolution and MODIS level-1 MOD021KM from collection 6, band 31, at 1000-m resolution were employed. No time correction was applied for the sensor overpass time, choosing the MODIS acquisition time at 10:00 a.m. and Landsat 8 overpasses at 10:33 a.m. The image data chosen to determine the blender (see Fig. 2) were acquired on 14th March 2016 and 20th July 2016. MODIS/TIR and L8/TIRS images were geometrically co-registered and resampled to the same pixel size and area and radiometrically calibrated, to ensure radiometric consistence. To this end, MODIS data were re-projected into WGS84 UTM projection system, the same as Landsat data products, using the MODIS Reprojection Tools and a bilinear resampling method. Moreover, a shared cloud mask was created for L8/TIRS and MODIS/TIR data on the selected dates to remove poor quality pixels.

The date chosen for the generation of the 10-m resolution image data was May 1st 2016. Accordingly, MODIS data on this date was used to apply the estimator and calculate the synthetic TIRS data resolution. Next, the unmixing algorithm was applied to estimate TIR radiance at 10-m spatial resolution. To generate the cluster map according to their VNIR reflectance, S2 MSI bands 2, 3 and 4 (corresponding to the visible range) on the required date (i.e. May 1st 2016) were used.

In addition, on May 1st 2016 a real L8/TIRS image was available, which was used to validate the proposed methodology. Fig. 5 illustrates the following images on May 1st 2016: the 1000-m resolution MODIS/TIR (Fig. 5a) and the L8/TIRS image at 30-m resolution used for validation (Fig. 5c). The final result (Fig. 5d) that is the synthetic 10-m resolution shows how well the higher spatial resolution captures the heterogeneity of the clouds. Overall, the shape of clouds in the synthetic 30-m and 10-m TIR image (Fig. 5b and c) is similar to the shape in the real 30-m resolution TIRS image (Fig. 5b), but many spatial details appear in the 10-m image only. In the visual evaluation of the synthetic 10-m resolution image, it should be taken into account that the unmixing in Step 2 is done by classifying both the L8/TIRS and the S2/MSI images within a small search window and then, assigning to the 10-m pixels within the window the TOA radiance values retrieved with L8/TIRS data for each class.

The stepwise improvement in the spatial resolution are evident when comparing the original MODIS TIR image (Fig. 5a) with the synthetic L8/TIRS image generated by Step 1 (Fig. 5b). The quality of the latter is clearly worse than the actual L8/TIRS image (Fig. 5c), which however is available on average once a month taking cloudiness into account, while a synthetic L8/TIRS image can be generated on any date required by users. Finally, the benefit of the linear un-mixing (Step 2) is evident in the synthetic MSI/TIR image at 10 m spatial resolution (Fig. 5d). It is worth nothing that the pixelized appearance of Fig. 5b is removed by the un-mixing, since the spatial patterns come from the

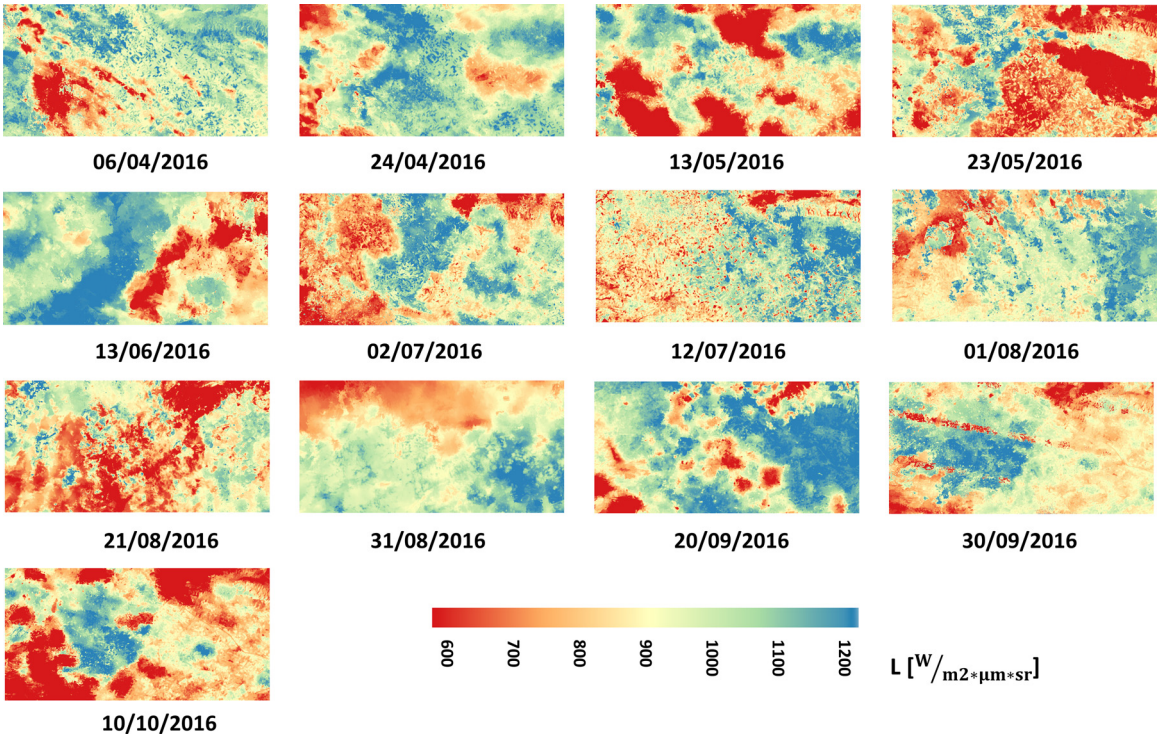

Fig. 6. Time series of synthetic TIR images at 10-m resolution in Northern Puglia (Italy) (DL coordinates: 511439, 4,590,240; UR coordinates: 568912, 4,619,213; EPSG 32,633).

Table 1
Dates of acquisition of image data applied to generate the time series of synthetic TIR images at 10 m resolution; Northern Puglia (Italy).

MODIS/TIR & L8/TIRS (t_1 and t_3) *(YYMMDD)*	MODIS/TIR & S2 MSI (t_2) *(YYMMDD)*
160331	–
160416	160406
160502	160424
160518	160513
160603	160523
160619	160613
160705	160702
160721	160712
160806	160801
160822	160821
160907	160831
160923	160920
161009	160930
161025	161010

multispectral MSI image at 10 m resolution, while the synthetic L8/OLI + TIRS image serves the purpose of providing estimates of the TOA radiance for each MSI pixel. The differences in spatial resolution between the images in Fig.5 become even clearer when magnifying the entire figure.

3.2. Demonstration case study: Northern Puglia (Italy)

A time series of synthetic TIR images at 10 m spatial resolution was generated for the period April to October 2016 over an area of 22 × 41 km^2 in the vicinity of Foggia in Northern Puglia (Italy) (Fig. 6).

To generate time series of synthetic TIR, we used (Table 1) the same combination of image data as in the previous case, with MODIS images acquired at 10:00 a.m., TIRS images at 9:40 a.m. and S2 MSI VIS bands at 9:54 am.

4. Result validation

4.1. Validation: The Netherlands

The observed MODIS/TIR image at 1000-m resolution (Fig. 7a) and L8/TIRS image at 30-m resolution (Fig. 7b) clearly contain different information, particularly the intermediate values of MODIS/TIR radiance seem to be due to spatial averaging of the radiance values captured by L8/TIRS, characterized by a bi-modal distribution. Three modes appear in the synthetic HR TIR image (10-m) (Fig. 7c), where the number of pixels in the lower radiance range, i.e. < 600, is underestimated when compared with the actual TIRS image. It is worth mentioning that MODIS radiances are higher than TIRS values due to different atmospheric conditions at acquisition time.

To validate the methodology, different tests have been performed. The synthetic 30-m TIRS image was compared first with the TIRS image observed on the same date (Fig. 8). Overall, the correlation was very high, i.e. 89%, showing a good similarity. To understand the differences between the two images, we generated the absolute difference image by subtracting the synthetic image from the real one (Fig. 8a) and the relative difference image (Fig. 8c). The distributions of absolute (Fig. 8b) and relative differences (Fig. 8d) show that differences are rather small in most pixels.

The distribution of absolute differences shows that the deviations are < 50 W/(m^2·µm·sr) for 59.33% of the pixels present a below and < 200 W/(m^2·µm·sr) for 95% of the pixels. The mean absolute error is 35.32 W/(m^2·µm·sr) and the mean relative error 8.51%, while the maximum error is less than 34% of the real value. Focusing on the spatial distribution of the differences, the larger errors may be explained by the different position of the clouds in the MODIS/TIR image and in the real L8/TIRS image (Fig. 5), which were acquired within 33 min, a time sufficient for the clouds to move a few kilometers. In addition, the larger MODIS pixel size, i.e. 1000 m vs the 30 m sampled L8/TIRS data increases the footprint of the clouds in the MODIS/TIR image compared with the L8/TIRS image, i.e. the larger pixel size works as a majority filter on the 30-m pixels. This leads to the appearance of

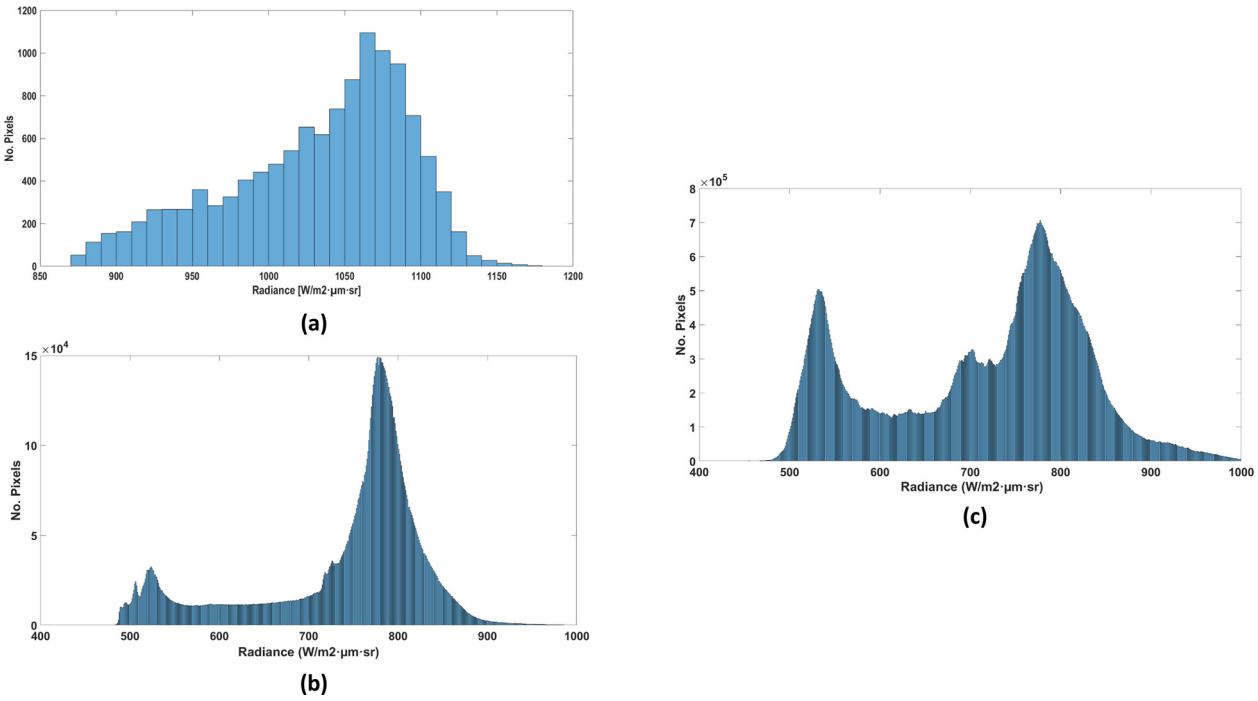

Fig. 7. Histogram of the observed MODIS/TIR band (a), of the observed L8/TIRS band-10 (b) and of the synthetic HR TIR image (10-m) (c) on the selected date (May 1st, 2016).

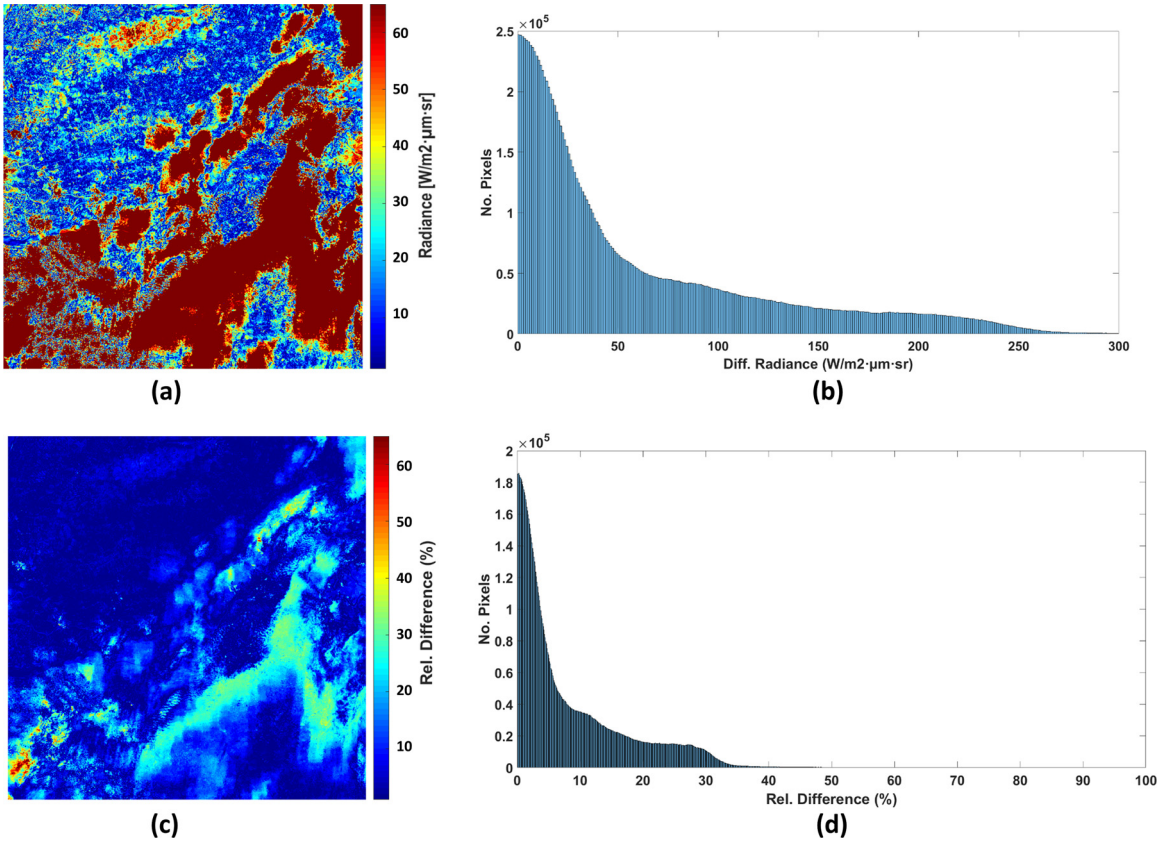

Fig. 8. Absolute difference radiance image in radiance values of the observed L8/TIRS image and the synthetic one (30-m) (a); histogram of absolute difference image (b); relative difference image (c); histogram of relative difference image (d).

cloud pixels in the synthetic image generated by applying the estimator to the MODIS data on the selected date. Pan et al. (2018) and Zaksek and Ostir (2012) performed a similar analysis of the constrained unmixing algorithm, showing a mean standard deviation of 8.5% in the first case, and 2.22 K (7.4%) in the second. It should be noted that the latter estimates of errors apply to the unmixing step only, while our

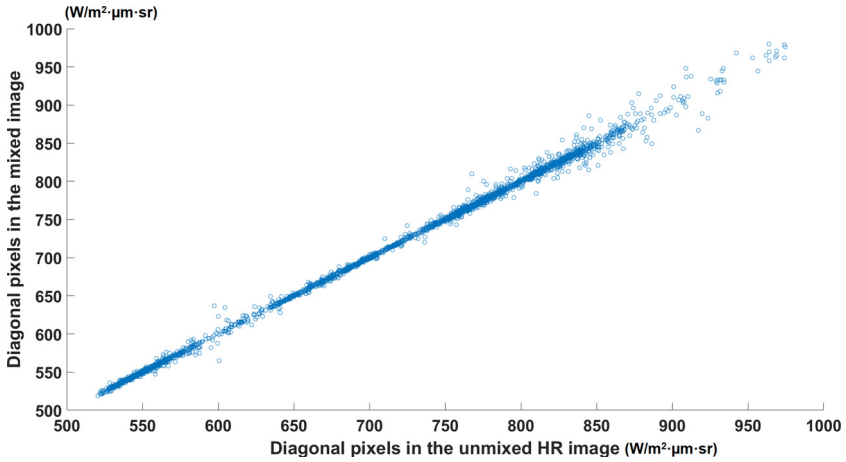

Fig. 9. Scatter plot of the diagonal profiles (DL to UR) from the synthetic HR TIR image (10-m) in *x* axis against the synthetic L8/TIRS image (30-m) in *y* axis.

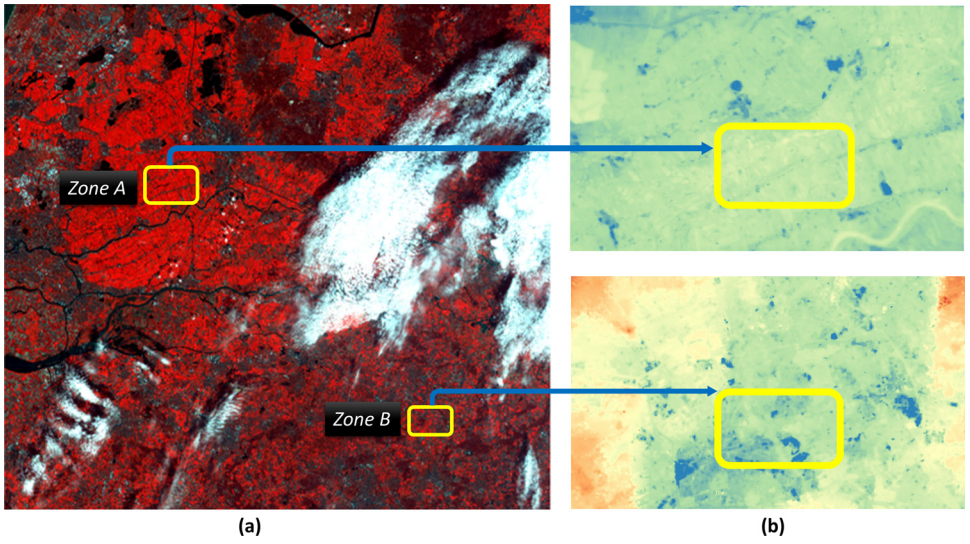

Fig. 10. Evaluation of the 30-m synthetic TIR image in The Netherlands: (a) Color composite of the L8/OLI at 30-m resolution; (b) zones A (upper panel) (DL coordinates: 626688, 5765164; UR coordinates: 634414, 5759892; EPSG 32631) and B (lower panel) (DL coordinates: 671780, 5699330; UR coordinates: 681992, 5706577; EPSG 32631) from the synthetic 30-m TIRS.

Table 2
Absolute error metrics in (W/(m^2·µm·sr) evaluated in zones A and B selected in the synthetic 30-m TIRS image of The Netherlands versus the actual L8/TIRS image on the selected date (May 1st, 2016).

Zone	MBE	AMBE	RMSE	RE	AE	η
A	−21.72	22.54	25.46	−2.77	2.88	0.055
B	−14.17	16.86	21.72	−1.75	2.09	0.549

errors apply to the full procedure (see Fig. 2), i.e. the generation of the TIRS image on the selected data, followed by unmixing.

We have also evaluated the synthetic HR TIR image (10-m) against the synthetic TIRS image (30-m). The correlation coefficient was 0.99, showing a complete similarity. A more detailed evaluation was carried out by comparing the diagonal pixel profile (from lower-left to upper-right) of both images. The evaluation is performed by extracting the diagonal pixels of the 30-m resolution image and one every three diagonal pixels of the 10-m resolution image. The correlation coefficient of the these samples was 99.4% and the scatter plot (Fig. 9) shows that radiance values were quite close to the 1:1 line.

We have evaluated our procedure under cloudy and not-cloudy conditions. In the evaluation of the entire area in The Netherlands, there are some clouds. The sub-areas A and B indicated in Fig. 10 by yellow frames are cloud free. For these areas, we have evaluated several error metrics (Table 2) by comparing the synthetic 30-m TIRS image with an actual L8/TIRS image on the same date. The Mean Bias Error (MBE), the Absolute Mean Bias Error (AMBE), the Root Mean Square Error (RMSE), the Relative Error (RE) and the Absolute Error (AE) were computed as follows (Eqs. (5)–(9)):

$$MBE = \frac{\sum_{i=1}^{n}(x_{sim}^{i} - x_{obs}^{i})}{n} \quad (5)$$

$$AMBE = \frac{\sum_{i=1}^{n}|(x_{sim}^{i} - x_{obs}^{i})|}{n} \quad (6)$$

$$RMSE = \sqrt{\frac{\sum_{i=1}^{n}(x_{sim}^{i} - x_{obs}^{i})^{2}}{n}} \quad (7)$$

$$RE = 100^{*}\frac{\sum_{i=1}^{n}(x_{sim}^{i} - x_{obs}^{i})/x_{obs}^{i}}{n} \quad (8)$$

$$AE = 100^{*}\frac{\sum_{i=1}^{n}|(x_{sim}^{i} - x_{obs}^{i})/x_{obs}^{i}|}{n} \quad (9)$$

where x_{sint}^{i} is the i-th radiance value of the synthetic image, x_{obs}^{i} is the i-th radiance value of the observed L8/TIRS image used as a reference and n is the number of pixels of the selected zone on the selected date.

In addition, the Nash and Sutcliffe index, η, is also computed according to Zhou et al. (2016) (Eq. 10); used in hydrological modelling to characterize the error related to the spatial heterogeneity:

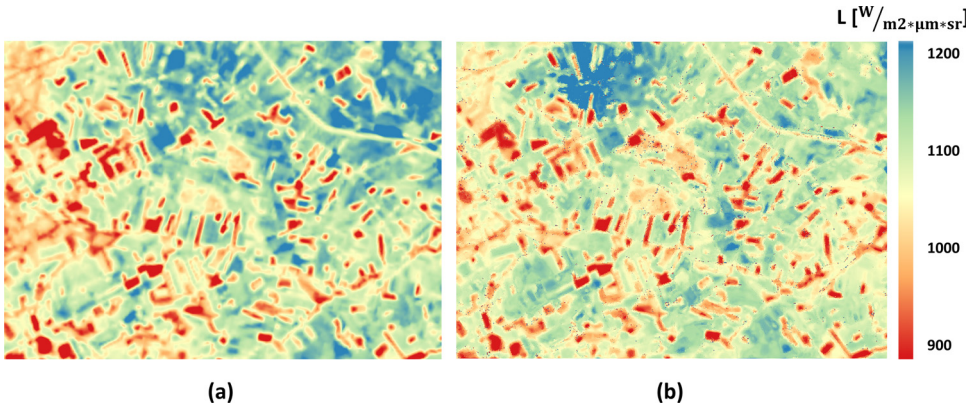

Fig. 11. TIR images on July 27th 2016: L8/TIRS at 30-m resolution (a) and synthetic TIR image data at 10-m resolution (b); (DL coordinates: 548307, 4591196; UR coordinates: 567863, 4606403; EPSG 32633).

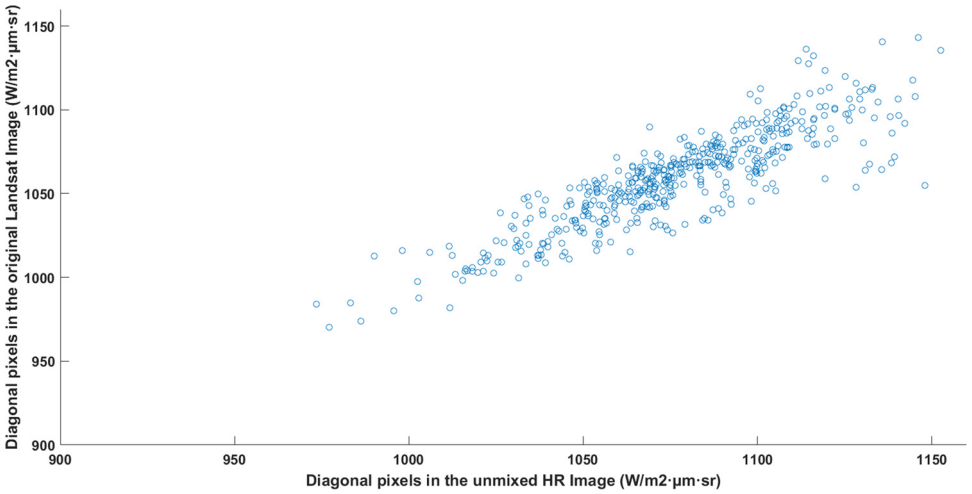

Fig. 12. Scatter plot of the diagonal pixels (Lower Left to Upper Right) in the original L8/TIRS image (Fig. 11a) against the diagonal pixels in the synthetic HR TIR image (Fig. 11b).

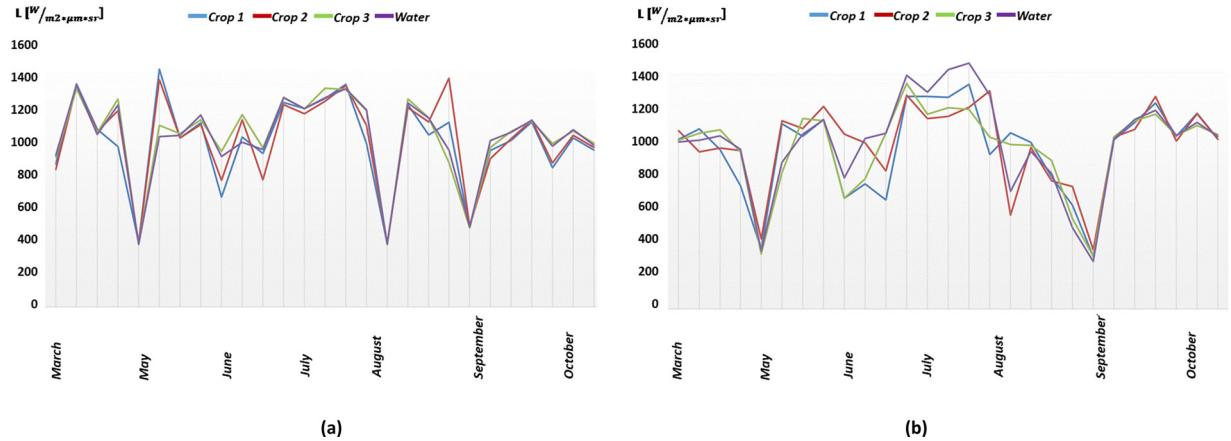

Fig. 13. Radiance time series for 2016 irrigation season for selected targets in Northern Puglia on the dates listed in Table 1: (a) MODIS/TIR (t_1, t_3 and t_2); (b) L8/TIRS (t_1 and t_3) and the synthetic HR TIR images (t_2) alternatively.

$$\eta = 1 - \frac{\sum_{i=1}^{n} (x_{sim}^{i} - x_{obs}^{i})^2}{\sum_{i=1}^{n} (x_{obs}^{i} - \bar{x_{obs}})^2} \quad (10)$$

where $\bar{x_{obs}}$ is the radiance value of the averaged observed image.

Zone A and B correspond to agricultural areas surrounded by rural regions, where thermal radiation is not influenced by complex terrain or by water bodies. In addition, these zones were chosen avoiding clouds at t_1, t_2 and t_3 (see yellow frames in Fig.10).

Table 2 shows the values of these absolute error metrics in (W/(m^2·µm·sr) evaluated for zones A and B. An 86% confidence level applies to these estimated errors. The radiance average within zone A is 780.129 W/(m^2·µm·sr), while within zone B is 793.415 W/(m^2·µm·sr).

To finalize with the discussion, in practice, the proposed methodology delivers an additional thermal band consistent with S2/MSI

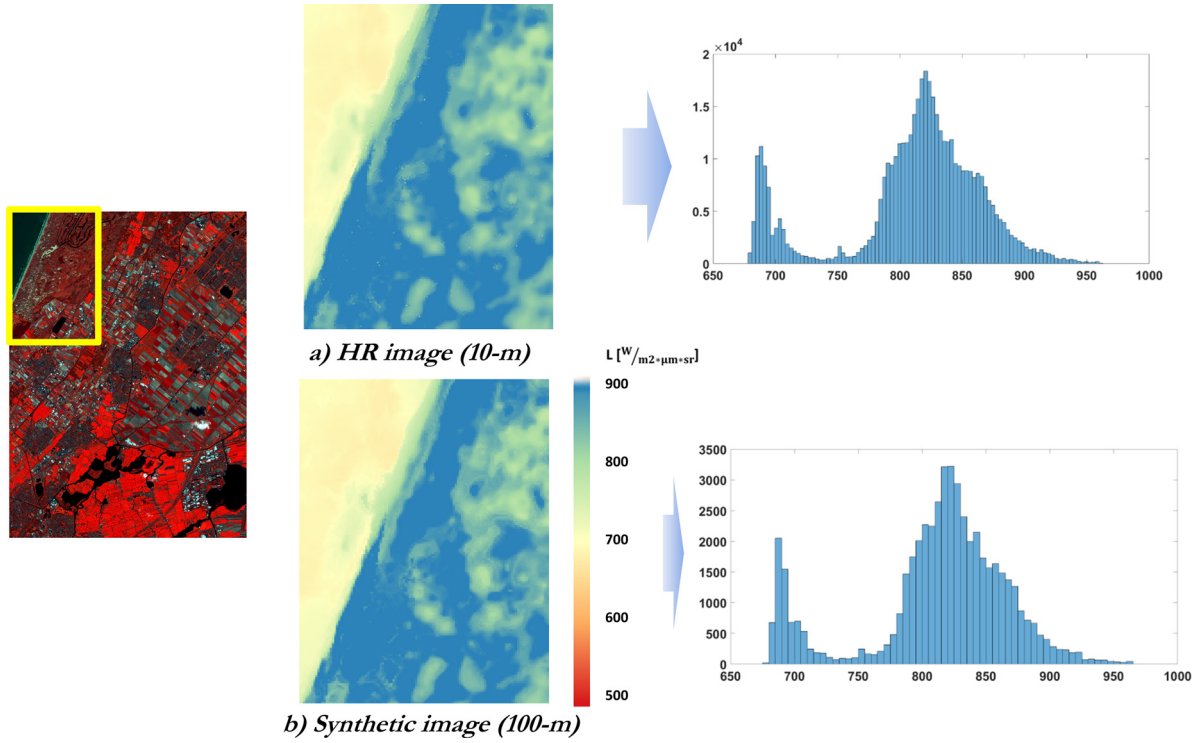

Fig. 14. High spatial resolution improvements in water-land transitions (The Netherlands).

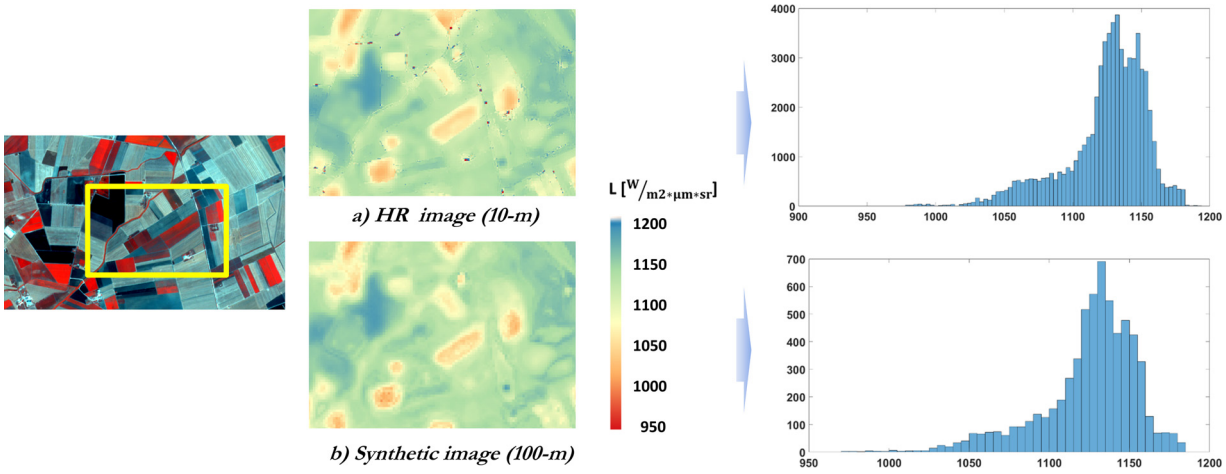

Fig. 15. High spatial resolution improvements in crop differentiation and delineation of irrigation channels (Northern Puglia, Italy).

bands at 10-m spatial resolution.

4.2. Demonstration: case study in Northern Puglia (Italy)

The time series images of Northern Puglia (Italy) from April to October 2016 was also evaluated. We have applied the proposed method and evaluated the radiometric performance of our downscaling procedure by selecting a cloud-free area of the image from 12/07/2016 in this time series, with a proper zoom to visually distinguish the improvements. Fig. 11 illustrates the following images on July 12st 2016: L8/TIRS image (Fig. 11a) and the synthetic 10-m TIR image (Fig. 11b). We compared the TOA radiance determined with our synthetic HR image (10-m) with the TOA radiance deterimed with an actual L8/TIRS image on this same date (12/07/2016) (Fig. 12). After that, a water body (549722, 4601341; EPSG 32633) and 3 different crops were chosen: crop 1 (556233, 4601437; EPSG 32633) and crop 2 (559794, 4605931; EPSG 32633) are vineyards while crop 3 (549319, 4605670; EPSG 32633) is cereals. These areas were chosen to avoid urban areas. We calculated the mean radiance for each target and date (see Table 1). The TOA radiance values measured by MODIS/TIR (Fig. 13a), L8/TIRS and synthetic HR TIR image (Fig. 13b) were rather similar in July and August, with the TIRS radiance somewhat lower from March through June. The seasonality was also clearer in the TIR observations at higher spatial resolution. As expected, differences acros targets were larger in the higher resolution images.

4.3. High spatial resolution details

A third evaluation focused on the synthetic HR TIR image (10-m). In the case of The Netherlands, the land-water boundary is delineated more accurately in the synthetic HR TIR image (Fig. 14a) than in the synthetic 30-m TIRS image (Fig. 14b). The histograms show that the HR image captures a mode around 700 W/(m^2·µm·sr), which is not visible in the 30-m resolution image. Similar comments apply to the details

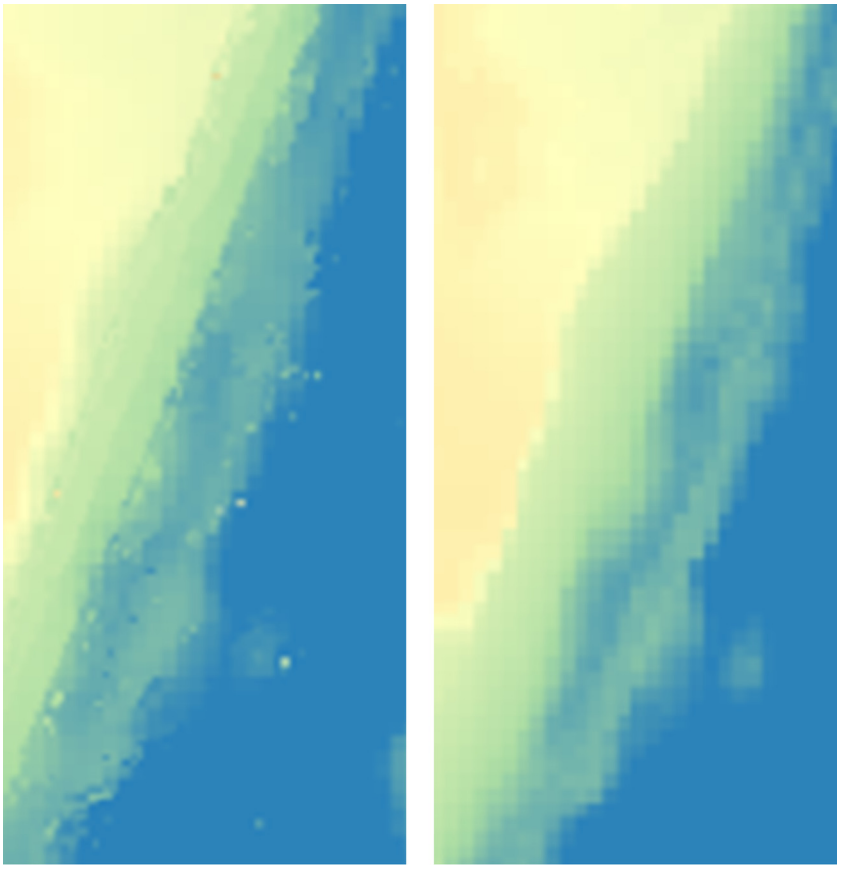

Fig. 16. Zoom in the study areas to illustrate the improvements from the step 2: (a) HR synthetic image (10-m), water-land transitions (The Netherlands), (b) Synthetic image (30-m), water-land transitions (The Netherlands).

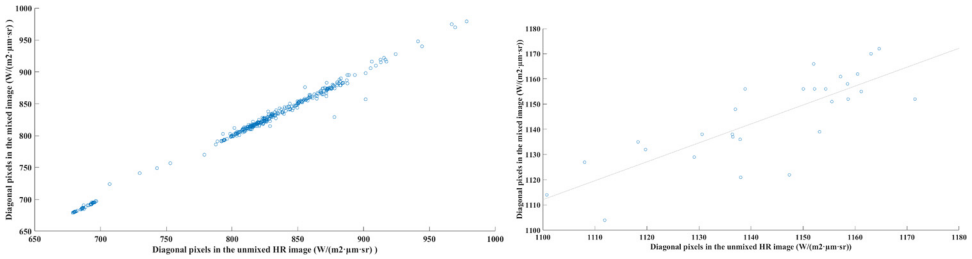

Fig. 17. Scatter plot of the diagonal pixels (Lower Left to Upper Right) sampled in the synthetic 30-m L8 TIRS image against the diagonal pixels in the synthetic 10-m TIR image (sample are from The Netherlands).

(Fig. 15) captured by the synthetic TIR image of Northern Puglia (Italy), where the crop differentiation and delineation of irrigation channels is better defined in the synthetic HR image.

A detail of the coastline (see Fig. 16) shows the improvement in spatial resolution achieved in Step 2.

To compare the radiance values in the images shown in Fig. 13 we sampled again the diagonal pixels (Lower Left to Upper Right) in the 30-m TIRS and 10-m TIR images. The data points sampled in the image of The Netherlands are rather close to the 1:1 line (Fig. 17).

5. Discussion

When the results are compared to those of other techniques, we find that most techniques are directly applied to the LST product, making the comparison difficult due to the different units of the error: Celsius degrees versus W/(m^2·µm·sr).

In comparison with methods where the regression models for the computation of the high spatial resolution TIR channel are based on the RGB and NIR channels from the same satellites, their advantage regarding the methodology proposed in this paper, is that the atmospheric correction is similar for all images, given that the acquisition hour is the same. For all downscaling techniques based on spectral indices such as NDVI, the regression with LST is calculated at coarse resolution and then applied to the computation of the new fine-resolution pixels. In addition, all techniques present a mean error around 2 °C for the downscaling of Landsat LST and 1.2 °C for downscaling MODIS LST, which, for the images under study, represent errors of 8% and 4.6% respectively. Results of the methodology presented in this paper are within the state of the art, with a mean error of 8.51% including both the generation of a synthetic image to increase temporal resolution and its downscaling. Last, it should be highlighted that methodologies based on NDVI are adequate for agricultural and vegetated scenes, while their

accuracy is reduced in mixed land cover regions, especially when water bodies are present.

For areas with water bodies, downscaling techniques for LST can rely on topographic data as their auxiliary source of information (Li et al., 2013), as topography can establish spatial limitations to the water extension. Spectral index such as NDWI (Normalized Different Water Index) are also useful in cases with water scenarios (Xiao et al., 2018). However, these techniques present average errors of 53%. This high value can be due to the difference between coarse and fine spatial resolutions (downscaling was performed for MODIS data from 500-m to 30-m resolution), but also due to the high uncertainty of the NDWI index used as auxiliary data. Similar results are obtained in (Bangira et al., 2017b) for downscaling MERIS data from 300-m to 30-m spatial resolution, where both NDWI and NDVI are combined in order to reduce the number of bands required as auxiliary data. In this case, the selection of pure pixels to determine the reflectance value of the endmembers for the unmixing algorithm has great influence in the results.

The advantage of the methodology presented in this paper regarding the previous techniques is that it is based on an unsupervised image classification, where classes are created from the radiance values present in the image, so it is adaptable to all scenes and consequently there is no limitation regarding admissible land covers.

However, existing downscaling methods only focus on the increase of spatial resolution, while the temporal resolution is not modified. This limitation implies that, for applications with need for high temporal resolution, downscaling has to be applied to images from satellites with high temporal resolution, which usually implies very low spatial resolution in all bands, limiting the final spatial resolution of the downscaling procedure. As an example, MODIS data presents the higher temporal resolution between open-access satellite data: the thermal band has 1000-m spatial resolution, while the RGB and NIR bands present a finest spatial resolution of 240 m, much higher than the 10-m spatial resolution obtained by the proposed methodology thanks to its multi-source nature (combination of data from different satellites).

6. Conclusions

The proposed methodology makes it feasible to generate TIR data products with both high spatial resolution and frequent coverage by combining radiometric data acquired by different imaging radiometers on different satellites, MODIS/TIR, L8/TIRS and S2/MSI in our study. Our method generates synthetic TIR images at the same spatial resolution as the target in the second stage of the approach, S2/MSI in our study. Such a capability is vital to monitor crop development during the growing season, given the fragmentation of most agricultural landscapes.

The synthetic TIR image and the observed L8/TIRS image gave a correlation coefficient of 0.89 and rather small absolute and relative errors on TOA radiance.

This approach has a few limitations. Features and temporal changes that are missed due to clouds or are not captured by the MODIS image on the selected date cannot be estimated and captured by the synthetic high resolution TIR image. The performance of the spatial unmixing algorithm depends on the quality of the clustering map, essentially on the separability and stability of classes mapped by the unsupervised procedure. The use 5-pixel moving window slightly reduces spatial variability in TOA radiance, since the unmixing procedure assigns the same radiance value to all pixels of the same cluster within the 5-pixel window.

Further studies will address how to fill up the missing values caused by clouds to generate the estimator (step 1). The effect of different moving window sizes and the extension of the clustering map from the unmixing algorithm (step 2) to multi-source data fusion with different spectral bands will be considered. Additionally, if the acquisition time between satellites considerably differs, short-term variations in TOA will need to be corrected for.

The method as described is applicable to any roughly similar combination of platforms and sensors as demonstrated in this study. What is needed is a platform providing daily or better thermal infrared image data, such as SUOMI/VIRS or Sentinel 3/SLSTR, one platform providing multispectral, including thermal infrared, data at higher spatial resolution occasionally concurrent with the lower resolution data such as ASTER or HJ-1 and one platform providing multispectral image data at very high spatial resolution such as GAOFEN-1.

Author contributions

M.M., M.H., S.L. and S.A. conceived and designed the experiments; M.H. and S.L. performed the experiments; M.M. and S.A. analyzed the data; all wrote and edited the paper.

Conflicts of interest

The authors declare no conflict of interest.

Acknowledgments

The research is partly funded by “Smart irrigation from soil moisture forecast using satellite and hydro-meteorological modelling (SIM)” from the waterworks 2014 cofounded call. Authors would also like to thank the Government of Spain for funding given through human resources programs (IJCI-2015-24492 and CAS16/00060).

References

Alfieri, S.M., Lorenzi, F.D., Menenti, M., 2013. Mapping air temperature using time series analysis of LST: the SINTESI approach. Nonlinear Process. Geophys. 20 (4), 513–527.
Ball, G.H., Hall, D.J., 1965. ISODATA, A Novel Method of Data Analysis and Pattern Classification. Stanford Research Institute, Menlo Park, United States. Office of Naval Research. Information Sciences Branch.
Bangira, T., Alfieri, S., Menenti, M., van Niekerk, A., Vekerdy, Z., 2017a. A spectral unmixing method with ensemble estimation of endmembers: application to flood mapping in the Caprivi floodplain. Remote Sens. 9, 1013–1035.
Bangira, T., Alfieri, S., Menenti, M., van Niekerk, A., Vekerdy, Z., 2017b. A spectral unmixing method with ensemble estimation of endmembers: application to flood mapping in the Caprivi Floodplain. Remote Sens. 9, 1013–1026.
Bechtel, B., Zaksek, K., Hoshyaripour, G., 2012. Downscaling Land Surface Temperature in an urban area: a case study for Hamburg, Germany. Remote Sens. 4 (10), 3184–3200.
Carlson, T., 2007. An overview of the" triangle method" for estimating surface evapotranspiration and soil moisture from satellite imagery. Sensors 7 (8), 1612–1629.
Corbari, C., Mancini, M., 2014. Calibration and validation of a distributed energy–water balance model using satellite data of land surface temperature and ground discharge measurements. J. Hydrometeorol. 15 (1), 376–392.
Dominguez, A., Kleissl, J., Luvall, J.C., Rickman, D.L., 2011. High-resolution urban thermal sharpener (HUTS). Remote Sens. Environ. 115 (7), 1772–1780.
Elsayed, S., Elhoweity, M., Ibrahim, H.H., Dewir, Y.H., Migdadi, H.M., Schmidhalter, U., 2017. Thermal imaging and passive reflectance sensing to estimate the water status and grain yield of wheat under different irrigation regimes. Agric. Water Manag. 189, 98–110.
Gao, F., Masek, J., Schwaller, M., Hall, F., 2006. On the blending of the Landsat and MODIS surface reflectance: predicting daily Landsat surface reflectance. Ieee Trans. Geosci. Remote. Sens. 44 (8), 2207–2218.
Guo, J., Tian, G., Zhou, Y., Wang, M., Ling, N., Shen, Q., Guo, S., 2016. Evaluation of the grain yield and nitrogen status of wheat (Triticum aestivum L.) using thermal imaging. Field Crops Res. 196, 463–472.
Handcock, R., Gillespie, A., Cherkauer, K., Kay, J., Burges, S., Kampf, S., 2006. Accuracy and uncertainty of thermal-infrared remote sensing of stream temperatures at multiple spatial scales. Remote Sens. Environ. 100 (4), 427–440.
Herrero-Huerta, M., Felipe-García, B., Belmar-Lizarán, S., Hernández-López, D., Rodríguez-Gonzálvez, P., González-Aguilera, D., 2016. Dense Canopy Height Model from a low-cost photogrammetric platform and LiDAR data. Trees 30 (4), 1287–1301.
Julien, Y., Sobrino, J.A., Mattar, C., Ruescas, A.B., Jimenez-Munoz, J.C., Soria, G., et al., 2011. Temporal analysis of normalized difference vegetation index (NDVI) and land surface temperature (LST) parameters to detect changes in the Iberian land cover between 1981 and 2001. Int. J. Remote Sens. 32 (7), 2057–2068.
Kim, M.S., Lefcourt, A.M., Chao, K., Chen, Y.R., Kim, I., Chan, D.E., 2013. Multispectral detection of fecal contamination on apples based on hyperspectral imagery. Part 1: application of visible and near-infrared reflectance imaging. Trans. Asae 45 (6), 2027–2037.
Kou, X., Jiang, L., Yan, S., Zhao, T., Lu, H., Cui, H., 2017. Detection of land surface freeze-thaw status on the Tibetan Plateau using passive microwave and thermal infrared remote sensing data. Remote Sens. Environ. 199, 291–301.

Kustas, W., Norman, J., Anderson, M., French, A., 2003. Estimating subpixel surface temperature and energy fluxes from the vegetation index-radiometric temperature relationship. Remote Sens. Environ. 85, 429–440.
Li, S., Sun, D., Goldberg, M., Stefanidis, A., 2013. Derivation of 30-m resolution water maps from TERRA/MODIS and SRTM. Remote Sens. Environ. 134, 417–430.
Masek, J.G., Vermote, E.F., Saleous, N.E., Wolfe, R., Hall, F.G., Huemmrich, F., Gao, F., Kutler, J., Lim, T.K., 2006. A Landsat surface reflectance data set for North America, 1990–2000. IEEE Geosci. Remote Sens. Lett. 3 (1), 69–72.
Menenti, M., Azzali, S., Verhoef, W., van Swol, R., 1993. Mapping agroecological zones and time lag in vegetation growth by means of fourier analysis of time series of NDVI images. Adv. Space Res. 13 (5), 233–2375.
Mukherjee, S., Joshi, P., Garg, R., 2014. A comparison of different regression models for downscaling Landsat and MODIS land surface temperature images over heterogeneous landscape. Adv. Space Res. 54, 655–669.
Mukherjee, S., Joshi, P.K., Garg, R.D., 2017. Analysis of urban built-up areas and surface urban heat island using downscaled MODIS derived land surface temperature data. Geocarto Int. 32 (8), 900–918.
Nash, J.E., Sutcliffe, J.V., 1970. River flow forecasting through conceptual models part I—a discussion of principles. J. Hydrol. 10 (3), 282–290.
Ning, J., Gao, Z., Meng, R., Xu, F., Gao, M., 2017. Analysis of relationships between land surface temperature and land use changes in the Yellow River Delta. Front. Earth Sci in press.
Pan, X., Zhu, X., Yang, Y., Cao, C., Zhang, X., Shan, L., 2018. Applicability of downscaling land surface temperature by using normalized difference sand index. Sci. Rep. 8, 9530.
Price, J.C., 1994. How unique are spectral signatures? Remote Sens. Environ. 49 (3), 181–186.
Richter, R., Schläpfer, D., Müller, A., 2006. An automatic atmospheric correction algorithm for visible/NIR imagery. Int. J. Remote Sens. 27 (10), 2077–2085.
Shabanov, N.V., Wang, Y., Buermann, W., Dong, J., Hoffman, S., Smith, G.R., et al., 2003. Effect of foliage spatial heterogeneity in the MODIS LAI and FPAR algorithm over broadleaf forests. Remote Sens. Environ. 85 (4), 410–423.
Smigaj, M., Gaulton, R., Suarez, J.C., Barr, S.L., 2017. Use of miniature thermal cameras for detection of physiological stress in conifers. Remote Sens. 9 (9), 957.
Sobrino, J.A., Jiménez-Muñoz, J.C., 2005. Land surface temperature retrieval from thermal infrared data: an assessment in the context of the Surface Processes and Ecosystem Changes through Response Analysis (SPECTRA) mission. J. Geophys. Res. Atmos. 110 (D16).
Stathopoulou, M., Cartalis, C., 2009. Downscaling AVHRR land surface temperatures for improved surface urban heat island intensity estimation. Remote Sens. Environ. 113 (12), 2592–2605.
Weng, Q., 2009. Thermal infrared remote sensing for urban climate and environmental studies: methods, applications, and trends. Isprs J. Photogramm. Remote. Sens. 64 (4), 335–344.
Weng, Q., Fu, P., Gao, F., 2014. Generating daily land surface temperature at Landsat resolution by fusing Landsat and MODIS data. Remote Sens. Environ. 145, 55–67.
Wu, P., Shen, H., Zhang, L., Gottsche, F.M., 2015. Integrated fusion of multi-scale polar-orbiting and geostationary satellite observations for the mapping of high spatial and temporal resolution land surface temperature. Remote Sens. Environ. 156, 169–181.
Xiao, F., Cheng, W., Zhu, L., Feng, Q., Du, Y., 2018. Downscaling MODIS-derived water maps with high-precision topographic data in a shallow lake. Int. J. Remote Sens. https://doi.org/10.1080/01431161.2018.1474529.
Xu, Y., Huang, B., Xu, Y., Cao, K., Guo, C., Meng, D., 2015. Spatial and temporal image fusion via regularized spatial unmixing. Ieee Geosci. Remote. Sens. Lett. 12 (6), 1362–1366.
Yue, W., Xu, J., Tan, W., Xu, L., 2007. The relationship between land surface temperature and NDVI with remote sensing: application to Shanghai Landsat 7 ETM + data. Int. J. Remote Sens. 28 (15), 3205–3226.
Zaksek, K., Ostir, K., 2012. Downscaling land surface temperature for urban heat island diurnal cycle analysis. Remote Sens. Environ. 117, 114–124.
Zhong, Y., Jia, T., Zhao, J., Wang, X., Jin, S., 2017. Spatial-spectral-emissivity land-cover classification fusing visible and thermal infrared hyperspectral imagery. Remote Sens. 9 (9), 910.
Zhou, J., Jia, L., Van Hoek, M., Menenti, M., Lu, J., Hu, G., 2016. An optimization of parameter settings in HANTS for global NDVI time series reconstruction. IEEE Int. Geosci. Remote Sens. Symp. 7729884, 3422–3425.
Zhukov, B., Oertel, D., 1996. Multi-sensor multi-resolution technique and its simulation. Zeitschrift Photogramm. Fernerkundung 1, 11–21.
Zhukov, B., Oertel, D., Lanzl, F., Reinhackel, G., 1999. Unmixing-based multisensor multiresolution image fusion. Ieee Trans. Geosci. Remote. Sens. 37 (3), 1212–1226.
Zurita-Milla, R., Clevers, J.G.P.W., Schaepman, M.E., 2008. Unmixing-based landsat TM and MERIS FR data fusion. IEEE Geosci. Remote Sens. Lett. 5 (3), 453–457.